Heritage Science

RESEARCH

Open Access

Bohemian sandstone for restoration of cultural heritage sites: 3D microstructure and mass transport properties

Pavel Capek[1], Martin Vesely[1], Milos Svoboda[2], Monika Remzova[3], Radek Zouzelka[3], Milan Kocirik[3], Libor Brabec[3] and Jiri Rathousky[3*]

Abstract

We characterised the microstructure of sandstone from the Msene locality (Czech Republic) by combining X-ray computed micro-tomography, back-scattered electron imaging, chemical composition analysis and textural analysis and gas permeation. Both, 2D and 3D images were commonly processed by linking an anisotropic non-linear diffusion filter and a segmentation method based on power watershed. This approach guaranteed binarised outputs that were almost the same in wide ranges of spatial-filter and power-watershed parameters, i.e., subjective choices of the parameters played the negligible role. The rock pore structure was found to be statistically homogeneous and almost isotropic with perfectly connected pore space. We also partitioned the void and solid phases into either grains or pores and throats, which enabled us to study characteristic sizes and connectivity of partitioned regions. By comparing pore and throat sizes, we demonstrated the significant convergent-divergent nature of the pore space because the throat size covered at most one half of the total surface area per pore (cavity). In addition, we calculated coordination numbers for all pores (cavities) to verify almost perfect connectivity of internal pores with those at the external surface. Effective (macroscopic) transport properties of the reconstructed pore space were simulated and the results were validated by experimentally observing steady state flow of inert gas. These findings appear to be a favorable starting point for future investigation of consolidation procedures. The well-connected pore structure with minimum occurrence of dead-end pores suggests that the consolidation agent is very likely to flood the whole pore space.

Keywords X-ray computed micro-tomography, BSE and EDS imaging, Partitioning of void and solid phases, Connectivity of phases, Effective transport parameters

Introduction

Porous sedimentary rocks are common materials of historical buildings and sculptural artifacts representing a highly valuable part of our cultural heritage. As their exteriors are exposed to destructive weathering due to the combined effects of humidity, acid gases (SO_2, CO_2, etc.), salt solutions and their crystallization in pores, and water freezing, efficient methods for their consolidation and protection are of major importance [1]. In our earlier study [2], we developed novel advanced consolidation agents based on alkoxysilanes and suspensions of nanoparticles in alkoxysilanes, the nanoparticles used posing no danger to human health and the environment [3]. The agents developed were found to cause a significant enhancement of the rock hardness. We can say that a substantial volume of empirical knowledge on the

*Correspondence:
Jiri Rathousky
jiri.rathousky@jh-inst.cas.cz
[1] Department of Organic Technology, Faculty of Chemical Technology, University of Chemistry and Technology, Prague, Technicka 5, 166 28 Prague 6, Czech Republic
[2] University of West Bohemia, Univerzitni 8, Pilsen, Czech Republic
[3] J. Heyrovsky Institute of Physical Chemistry of the CAS, Dolejskova, 2155/3, 182 23 Prague 8, Czech Republic

consolidation of porous stones has been accumulated so far (e.g., [4, 5]).

As in the restoration of weathered monuments the pore space of building materials is impregnated with liquid consolidation agents, the investigation of non-stationary transport phenomena is of utmost importance. Besides fluid properties, their complexity depends on the geometry as well as the topology of the pore space. Despite the progress achieved, the mechanism of the air displacement by the liquid consolidant and its adhesion to pore walls is poorly understood. In principle, the displacement proceeds via the reactive flow of the consolidant precursors into pores and the subsequent flow of solvent vapours out of pores. The process is accompanied by strong changes in fluid viscosity and surface tension. To get a deeper insight into the microscopic mechanism of consolidation, a study performed with a simpler and better-defined model system is desirable.

Based on our previous study into the consolidation [6], the sandstone from the locality Mšené, Czech Republic, was selected as a convenient candidate for a detailed study. In the past, this sandstone was used to restore some parts of, e.g., the St. Vitus Cathedral and Charles Bridge, which are the monuments of the highest importance in Prague [7]. As its content of quartz is more than 95 wt.%, the solid portion can be considered a single phase which simplifies the pore surface wetting. Another simplification in our study is that the pair of immiscible fluids subject to imbibition is gas (air, N_2) and water. It should be noted that in a recent paper, a sophisticated software Palabos: Parallel Lattice Boltzmann Solver was described as suitable for the solution of fluid dynamics problems of imbibition and consolidation of porous materials [8].

The principal aims of the present work are threefold. First, we reproduced the three-dimensional microstructure of the Mšené sandstone (i.e., a replica), by means of the X-ray computed micro-tomography. This information was combined with complementary data obtained by electron microscopy operated in the backscattered electron mode and energy-dispersive X-ray spectroscopy. The primary data from imaging were d finally converted into an indicator function for pore space. This is the final digital form of the pore space image serving as the input data for the simulation of fluid dynamics using appropriate software. Second, the digital images were analyzed by statistical methods to evaluate pore size distribution, pore connectivity, percolation properties of pore space, and other important microstructure characteristics, such as the petrographic characteristics of grains. Third, we compared effective (macroscopic) transport parameters of the sandstone from permeation measurements of inert gases with those obtained from simulated single-phase flow in the reconstructed pore space. The comparison of computed data with those from experimental measurements proved the model consistency.

Materials and methods

Sandstone samples and their basic characterisation

Sandstone samples from the Mšené locality, Czech Republic, were provided by the company Stone Carving and Restoration Pánek, Ltd., Czech Republic. Chemical composition of this sandstone is shown in Table 1. Rybařík [7] explored petrographic properties of the sandstone. It is a white-greyish clastic fine-grained sedimentary psammitic rock containing quartz as the dominant phase (95%), while the minority phases are muscovite and feldspar clasts. Cement is formed by clay minerals (kaolinite, chlorite, illite) but its content is very low.

Sandstone cubes with size of $50 \times 50 \times 50$ mm^3 (see Fig. 1) were machined from the delivered large bricks. Their faces with outer normal parallel to the direction of sedimentation (basal faces) were specified by the provider. Since some experimental methods required smaller samples (mercury porosimetry) and/or specific shapes (X-ray tomography and permeability measurement), some cubes were divided further into a number of rectangular parallelepipeds and cylinders. Their specific sizes are reported in the following text, technique by technique.

Initially, we applied the water imbibition (water absorbability) method [9] to evaluate open porosity of ten samples labelled A–J. The method allowed us to compare their open porosity values and to select representative samples. Detailed results are collected in Additional file 1 (SI). Since sample E was the most stable in terms of the relative change of its mass and since its open porosity ($\phi_w = 0.2742$) was close to an average value of 0.2715, we selected this sample (≡ specimen) to fulfil the principal aims of the study.

Open porosity and specific area of specimen E

The next textural characterisation of specimen E was carried out using a helium pycnometer AccuPyc II 1340,

Table 1 Chemical composition (wt.%) of the Mšené sandstone as published by Rybařík [7] (measured by X-Ray fluorescence)

SiO_2	Al_2O_3	K_2O	SO_3	Fe_2O_3	CaO	MgO	TiO_2
95.30	2.28	0.89	0.35	0.30	–	0.12	0.11

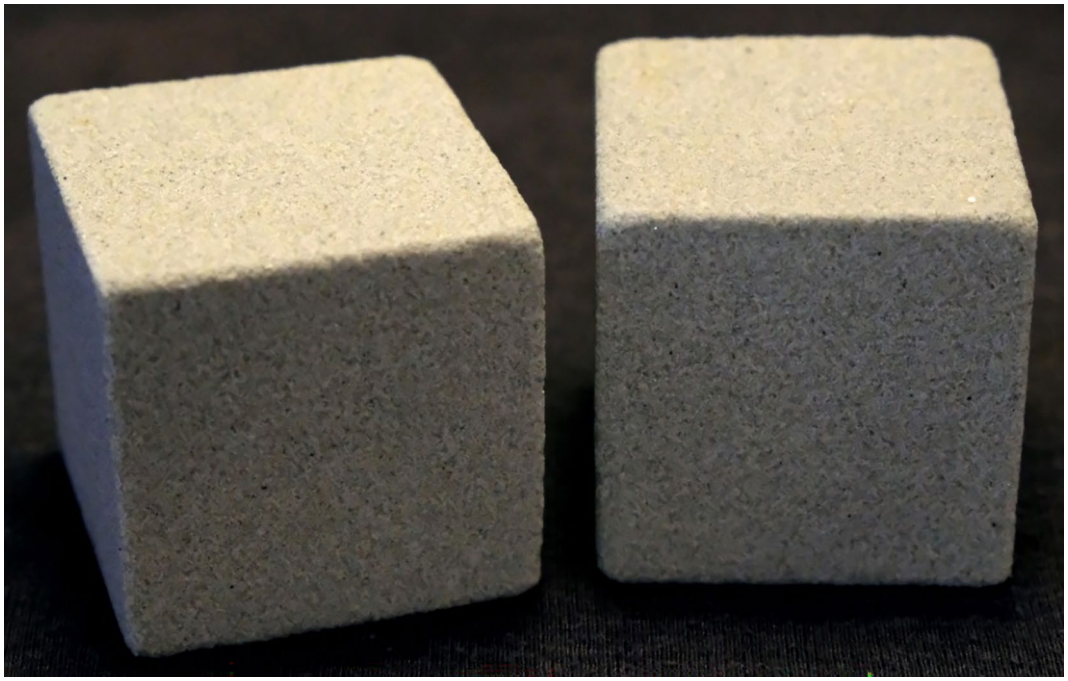

Fig. 1 Photographs of sandstone cubes with size of 50 × 50 × 50 mm^3 serving as the primary specimens

a mercury porosimeter AutoPore IV 9520 and a low-temperature pressure sorption analyser ASAP 2020 (all instruments by Micromeritics, USA). The samples were dried at a temperature of 150 °C for 4 h before textural analysis. The bulk and skeletal densities, ρ_b and ρ_s, the total open porosity ϕ_e, and the specific surface S_{BET} are collected in Table 2. Note that the skeletal densities calculated from the mercury intrusion and helium pycnometry slightly differed from each other, which also resulted in the small differences between the derived total open porosity. Since the specific surface was supposed to be very small, we repeated the measurements with nitrogen and krypton and compared the results.

The distribution of pore radii derived from the mercury intrusion curve is shown in Fig. 2. Its course points to an almost monodisperse pore structure with most of its volume located around a pore radius of 13.7 μm. A minor part of the total pore volume, specifically less than 5%, consists of narrower pores (with radius $r_p \leq 1.5$ μm) that account for the large BET specific surface relative to the prevailing macro-porosity. This observation was of primary interest because the smallest microstructural details that we could observe in an X-ray tomography volume image were limited by the size of cubic voxel that was approximately 2.6 μm wide (see the next sections). Consequently, micropores, mesopores, narrow macropores and small-scale surface roughness could not be observed in the X-ray tomography volume image of the sample. Due to this restriction we anticipated a discrepancy between s_e and the corresponding quantity calculated using the tomographic volume image.

Backscattered electron (BSE) imaging

Prior to X-ray imaging, a pore structure and a chemical composition of specimen E were observed in a Tescan Lyra3 GMU combined ion and scanning electron microscope equipped with detectors for BSE and EDS. First, two cubes of size 10 × 10 × 10 mm^3 were cut out of the pristine block. The cubes were dried and impregnated under vacuum with epoxy resin Struers EpoFix. The hardened epoxy resin blocks were cut, ground, and polished to achieve smooth surfaces of cross-sections

Table 2 Textural characteristics of specimen E and the derived quantities $\varphi_e = 1 - \rho_{b,Hg} / \rho_s$ and $s_e = S_{BET}\, \rho_{b,Hg}$

$\rho_{b,Hg}$, g cm^{-3}	$\rho_{s,Hg}$, g cm^{-3}	$\rho_{s,He}$, g cm^{-3}	S_{BET}, m^2 g^{-1}	$\varphi_{e,Hg}$, -	$\varphi_{e,He}$, -	s_e, mm^{-1}
1.9068	2.6332	2.6061	0.049	0.2759	0.2683	93

The mass of the samples was 1.0860 g, 0. 8487 g and 4.2479 g for helium pycnometry, mercury porosimetry and nitrogen sorption, respectively

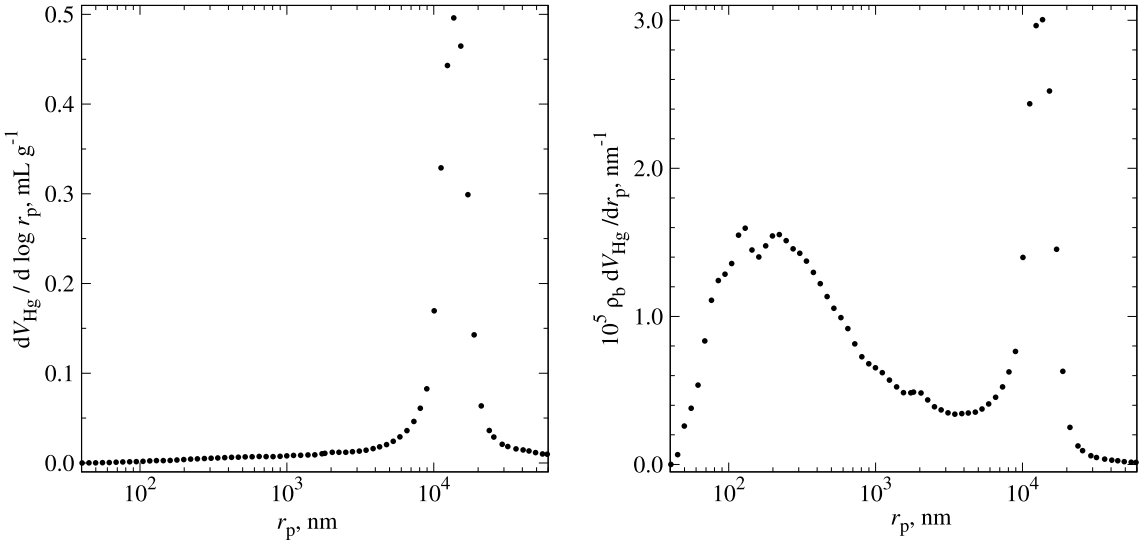

Fig. 2 Distribution of pore radii derived from mercury intrusion porosimetry assuming an advancing contact angle of 130°. The left chart uses the common quantity on its ordinate, while the right one shows the distribution with the transformed ordinate, $\rho_b\, dV_{Hg}/dr_p = (\rho_b/\ln(10)/r_p)\, dV_{Hg}/d\log(r_p)$, to stress the existence of narrower pores

through the resin blocks. Layers of gold with a thickness of 10 nm were sputtered on the polished sides of the resin blocks to increase their conductivity. Second, the electron beam was accelerated using a voltage of 10 kV, which ensured good contrast between the void (epoxy) and solid phases. All BSE images were recorded in an 8-bit grey intensity and a uniform size of 1024×1024 pixels. The size of a square pixel size was determined by trial and error: a final size of 2.44 μm was selected, as this ensured a reasonable balance between microstructural details and statistical significance of the major microstructural features (pores and grains) in the view field. Third, thick layers (0.2–1.0 mm) were cut off from of the resin blocks to observe other parts of the specimen and the whole process was repeated until a sufficiently large set of BSE images was obtained.

The grey intensity of each pixel carries information about the atomic numbers of the elements prevailing in the area on which the narrow beam of electrons is focused. The higher the atomic number, the brighter the pixel appears. This fact allowed us to distinguish between pores full of the epoxy resin, which were black or dark grey, and the solid phase, which was light.

Chemical composition analysis (elemental mapping) was carried out using the energy dispersive spectroscopy (EDS) analyser with an 80 mm^2 SDD detector (X-MaxN, Oxford instruments). An acceleration voltage of 15 kV was used in this case.

X-ray imaging

A cylinder with a diameter of 5 mm and a height of 7 mm was cut out of the pristine sandstone cube (specimen E). The specimen was scanned by an Xradia MicroXCT 400 device which is specialized for low absorbing materials with high resolution and uses a low voltage X-ray source (20–90 kV) combined with interchangeable high-resolution detectors. Positions of the source and the detector are stable during the scanning, while the sample is rotated step by step by 360 degrees about its vertical axis. A 2D transmission image is recorded in every set position. The parameters of scanning were the following: source voltage 45 kV, source power 4.5 W, pixel size 2.59 μm, detector resolution 2032×2032 pixels (binning 1), rotation angle 360°, number of images 1800, exposure time of each image 10 s, total scanning time 6.5 h, temperature 28 °C. The set of acquired transmission projections was processed by the XMReconstructor software, resulting in a volume image consisting of cubic voxels with a linear size of 2.59 μm. The volume image was stored as a stack of 2D tomographic TIFF images. One of them is shown in Fig. 3.

A cuboid region of size $1250 \times 1300 \times 1200$ voxels that fitted in the cylindrical volume image of the specimen was cut out and the resulting grey-scale volume image was processed further as described below. The axis of the cylindrical specimen was aligned with the *z*-axis of the cuboid region.

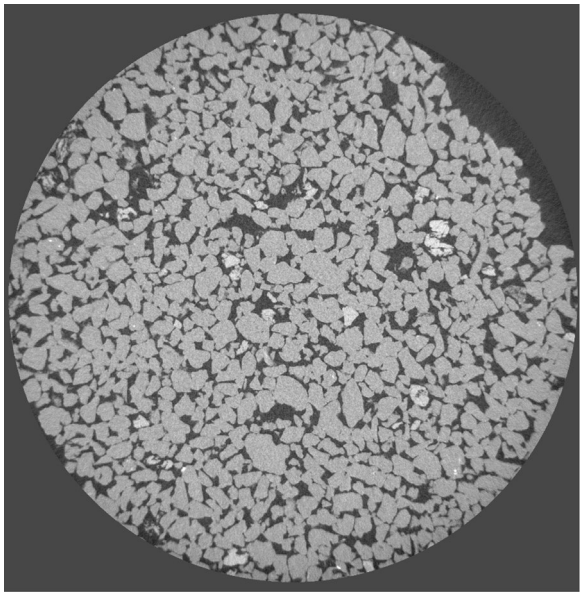

Fig. 3 A slice taken from the original grey-scale tomogram. The whole window has the size 1988 × 2032 pixels. The pixel size corresponds to the voxel size, i.e., $a = 2.59$ µm. While dark regions within the circular disc represent pores, the solid phase is more or less light grey

Filtering in the spatial domain and segmentation

A sequence of three spatial filtering steps included an adaptive median filter, a linear diffusion filter and an anisotropic non-linear diffusion filter. The adaptive median filter used a gradually growing spherical neighbourhood of a voxel under consideration to determine if a grey level of the voxel represented impulse noise. If it did, the median value deduced from the neighbourhood replaced the impulse noise grey level. Otherwise, the grey level of the voxel remained unchanged. After median filtering, the image was very gently smoothed by linear filtering in a very short time interval. This preliminary use of the linear diffusion filter allowed us to reduce the extent of internal smoothing associated with the anisotropic non-linear diffusion filter that carried out the major part of image processing prior to segmentation. We selected an edge enhancing filter that combined a reasonable computing complexity and a good performance [10–13]. The filter recognised phase interfaces between the solid and void phases and inhibited the transfer of grey levels across the interfaces, while a similar transfer in more or less homogeneous regions was enabled. This resulted in a smoothed volume image with sharpened phase interfaces.

Complete segmentation, i.e., separation of an image in a set of disjoint regions corresponding uniquely with foreground and background objects, was relatively easy once the smoothed images were ready. Since the edge-enhancing filter delivered, in fact, the partially segmented image, the problem of segmentation could be solved successfully using lower-level processing, e.g., using global grey-level thresholding. In this method a pixel/voxel is assigned to either foreground objects or background objects according to a single grey level, which is often derived from a grey-level histogram. In order to verify the uniqueness of segmentation, we repeated the task using a region-based method, specifically power watershed [14]. Power watershed combines the graph cut, random walk and shortest path optimisation algorithms. Since the power watershed algorithm needed an initialisation step generating foreground and background seeds, we accomplished this by using geodesic reconstruction from markers [15]. These procedures were identically used for both kinds of images—the two-dimensional BSE images and the X-ray volume image.

Description of pore structure

Each voxel/pixel of the segmented volume image belonged to either the void phase or the solid phase. This fact was mathematically expressed in terms of the indicator function for the void phase (pores) [16]

$$\mathrm{I}^{(\mathrm{v})}(\boldsymbol{x}) = \begin{cases} 1, & \text{if } \boldsymbol{x} \in \mathrm{V_v} \\ 0, & \text{otherwise} \end{cases} \tag{1}$$

where $\boldsymbol{x}$ is the position vector in the cuboid region V representing the volume image, i.e., $\boldsymbol{x} \in \mathrm{V}$ and $\mathrm{V} = \mathrm{V_v} \cup \mathrm{V_s}$ where $\mathrm{V_v}$ is the pore space and $\mathrm{V_s}$ is the region of the solid phase. Since the original image is digital (discrete), the position vector is also defined in the discrete space associated with a cubic lattice, i.e., $\boldsymbol{x} = (a\,i, a\,j, a\,k)$, where a stands for the voxel size. The integers i, j and k take values from the intervals $[0, l_1 - 1]$, $[0, l_2 - 1]$ and $[0, l_3 - 1]$ where l_1, l_2 and l_3 are the linear sizes of the cuboid region V. In the 2D space the definitions are analogous: $\boldsymbol{x} = (a\,i, a\,j)$ and $i \in [0, l_1 - 1] \wedge j \in [0, l_2 - 1]$.

The indicator function completely describes the digital pore structure (microstructure) of the sample. Its statistical characteristics reduce the amount of included information and offer a convenient computational link between the pore structure and macroscopic (effective) properties. The relevant statistical characteristics (descriptors) discussed in the following sections are described in the Additional file 1. Note that the indicator function of the sandstone is further called the replica.

Simulation of Knudsen diffusion and viscous flow in pore structure

Steady-state flow of single gas was simulated in the Knudsen region and in the region of continuum for

basic transport characteristic of the pore structure to be obtained, i.e., the effective pore size κ and the permeability β. In the first case, a random walk algorithm used the well-known relationship between the mean squared displacement of a walker and time. The resulting parameter—the effective pore size κ—characterise the conductivity of a pore medium for gases in the limit of molecular streaming or Knudsen flow. In the latter case, slow incompressible isothermal flow is governed by the Stokes equations that are solved numerically. After data reduction, the parameter β (permeability) measures the conductivity of a porous solid for fluids in the region of continuum. Details can be found in the Additional file 1.

Experimental determination of gas permeability

Permeation of pure inert gases was carried out in a modified apparatus whose original version was described by Fott and Petrini [17]. The flow of nitrogen or argon through a porous medium (plug) is observed in a quasi-stationary regime, the assumption of which is justified because pores in the porous medium has a negligible volume in comparison with volumes of the apparatus. Primary experimental data are collected in the form of transient pressure differences measured between the porous plug bases. Their statistical treatment estimates the effective pore size κ and permeability β. Details can again be found in the Additional file 1.

Results and discussion

BSE images of polished cross-sections of the specimen are discussed first, then elemental composition revealed by means of EDS is used to account for peculiarities (bright spots) in BSE and tomographic volume images, and the analysis of the tomographic volume image finishes the description of the specimen. For the tomographic data, a number of morphological descriptors are calculated to describe the microstructure comprehensively. In addition, macroscopic transport properties derived from the 3D pore structure are evaluated and compared with their experimental counterparts.

Two-dimensional microstructure

Imaging in the BSE mode gave the initial information about the microstructure. We exemplify the entire image processing in Fig. 4 where the same region of the raw, filtered and segmented image is shown. To stress the quality of the whole process, we also combined the raw image with white curves representing the phase interface (Fig. 4, bottom right). Most of the grains exhibited more or less rounded cross-sections, sometimes with sharp corners.

The specimen also contained small inclusions of heavier elements that created areas brighter than the surroundings. For this reason, a closer inspection using the EDS detector revealed that the specimen consisted of two main minerals, particularly quartz framework grains and alkali (potassium) feldspar grains, and small, rarely occurring inclusions containing titanium as the prevailing metal (43 − 54 wt.%) and iron traces (2.2 − 7.6 wt.%), which could be accounted for by the occurrence of rutile and ilmenite minerals. Simultaneous occurrence of aluminium, silicon and potassium (9.7 wt.% Al, 29.5 wt.% Si and 11.7 wt.% K) on the same spots marked the feldspar grains, while quartz grains were almost free of other elements different from silicon and oxygen. The titanium inclusions in the EDS map were identical to very bright parts of the BSE images. EDS maps are shown in Fig. 5.

Three-dimensional microstructure

Since details of spatial filtering and segmentation of the volume tomogram can hardly be shown in the 3D space, results of the individual operations are shown in the 2D space, see Fig. 6. It is worth noting that pore shapes seen in the CT grey-scale images can be directly compared with those coming from BSE imaging in Fig. 4.

In order to illustrate typical three-dimensional shapes of pores, we cut out of the whole segmented volume image ($\equiv$ primary replica with size of $1250 \times 1300 \times 1200$ voxels, i.e., $3.237 \times 3.367 \times 3.108$ mm^3) a small central region with size of 256^3 voxels (Fig. 7). This choice of size ensures that the resolution and size are balanced.

Microstructural analysis of the primary replica started with clustering void and solid voxels using 26-neighbour and 6-neighbour rules, respectively. In principle, the solid phase has to form a single large cluster to represent a physically realisable medium. Indeed, there was a large cluster of solid voxels that spanned the medium in all three principal directions. Due to the cuboid region cut out of the original volume image of the cylindrical specimen and imperfections of the whole imaging process, isolated clusters of the solid-phase voxels were found in the cuboid region. Those isolated clusters that were located at the replica boundaries were considered physical as a result of cutting out, while those being completely inside the replica were clearly created by local failures of the imaging process. The average volume of the internal isolated clusters was about 1.73 voxels, which suggested their origin in image processing rather than in the true structure. Therefore, the internal isolated clusters were removed, which slightly increased the total porosity (Table 3).

By contrast, the existence of isolated clusters of the void-phase voxels is physical and can easily be confirmed by means of X-ray tomography. Nevertheless, the particulate nature of the specimen reduced the probability that isolated pores could exist in the specimen. Cluster analysis revealed that the volume fractions of internal

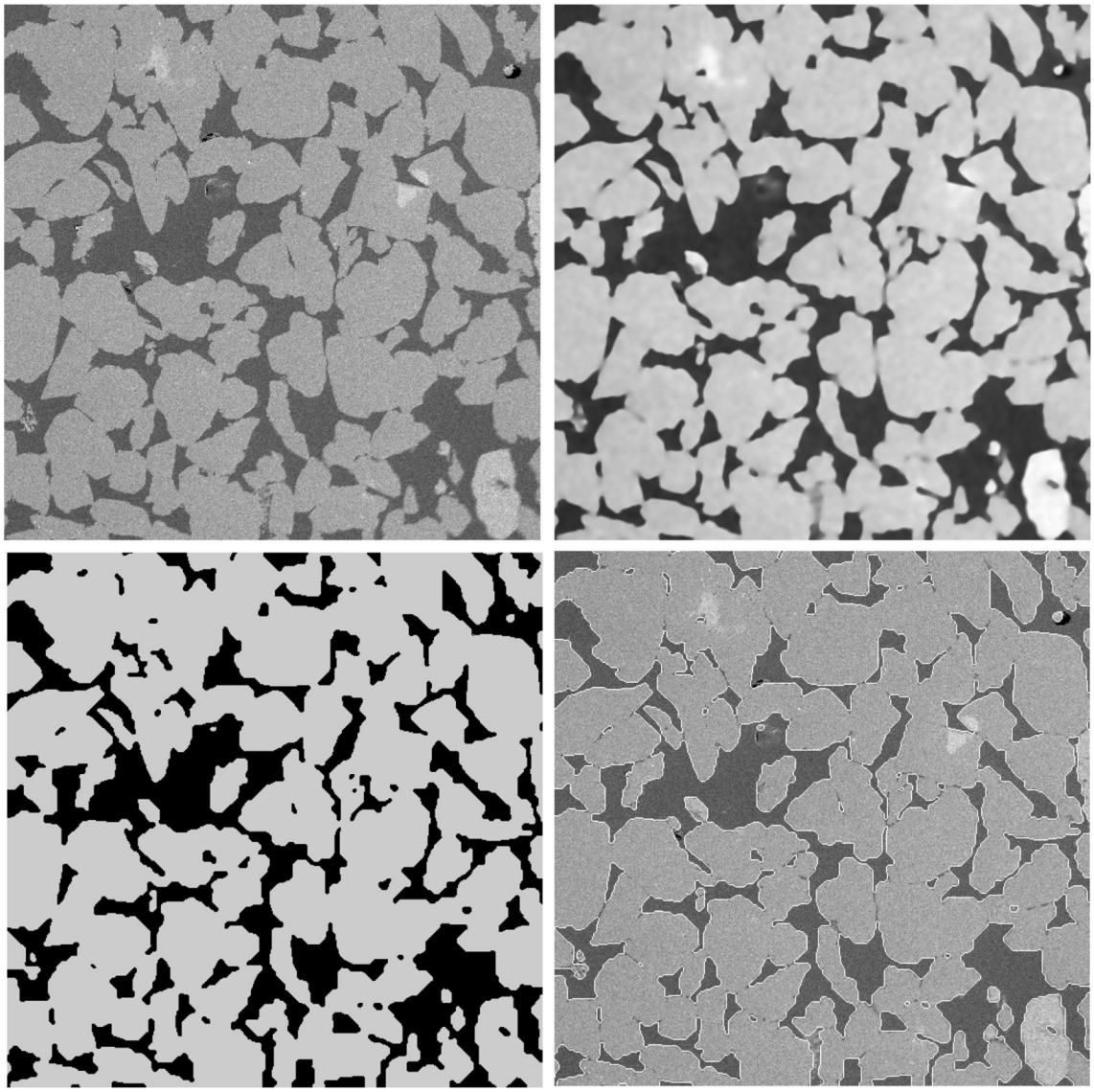

Fig. 4 Example of BSE imaging ($a = 2.44$ µm). The same region with a size of 512 × 512 pixels (one quadrant of the whole image) is shown for clarity. The raw and filtered images are displayed in the upper row, the segmented image and the combination of raw images with inscribed phase interfaces (bright white curves) are shown in the lower row (pores are black)

isolated clusters of both phases were approximately the same (Table 3). These facts gave us the opportunity to replace all internal isolated clusters of the void phase with volume less than 2000 voxels by the solid phase and to counterbalance the increase of the void fraction due to the removal of the isolated solid clusters. As a result, the smoothed pore structure (≡ secondary replica) had a total porosity of 0.272515, while the internal isolated clusters of solid voxels disappeared completely and the volume fraction of the internal isolated pores was less than 1.85×10^{-5}.

It is also worth noting that the smoothing changed the interface area per unit volume negligibly. This quantity calculated for the primary replica and the secondary replica are 34.5 mm^{-1} and 34.1 mm^{-1}, respectively. In addition, both 3D values are not far from the value obtained by processing the 2D BSE images, i.e., the result reads $23.9 \times 3/2 = 35.9$ mm^{-1} when the different values of d in Eq. (2) (see Additional file 1 SI) are taken into account. In the following discussions, only the secondary replica is used.

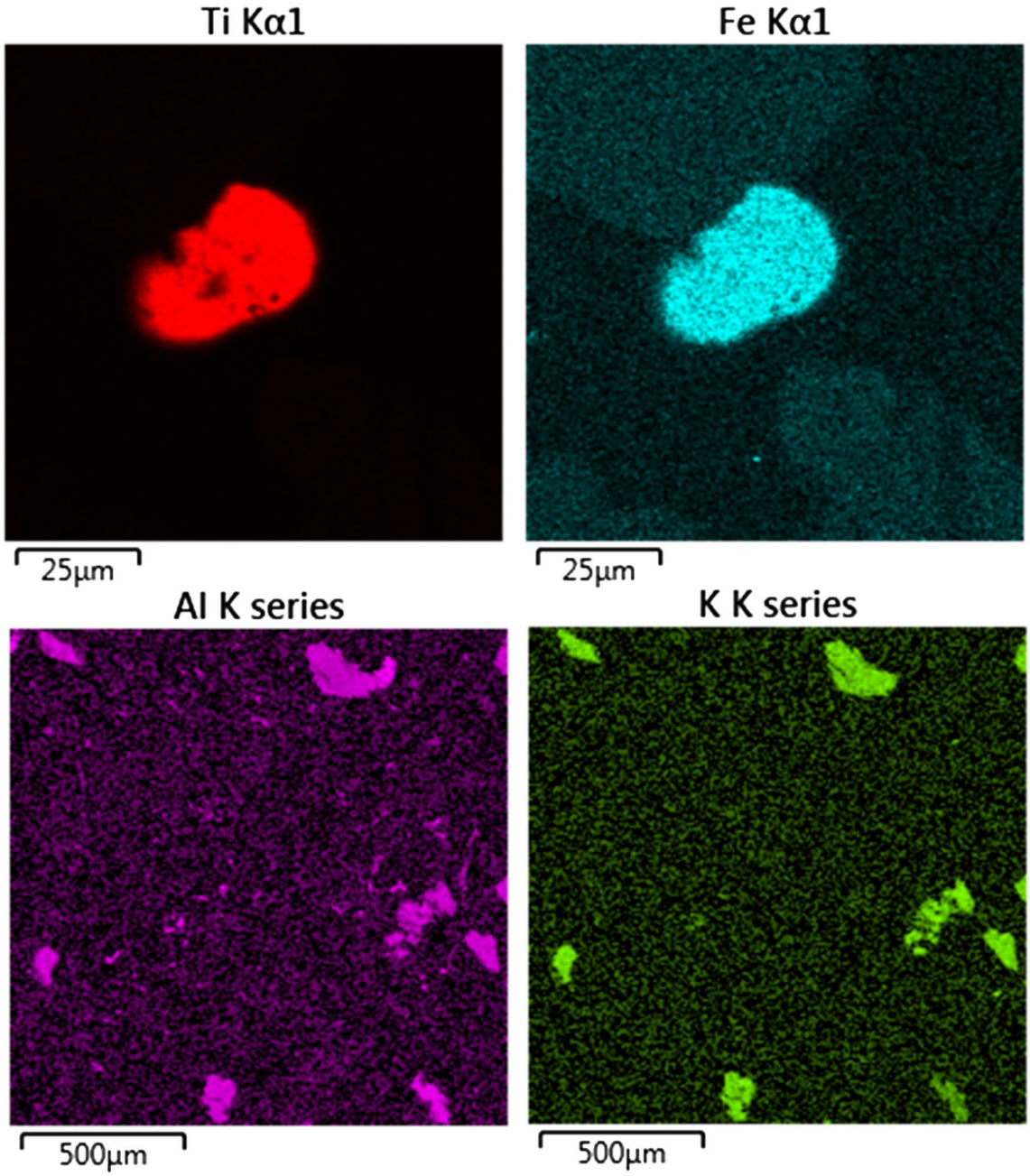

Fig. 5 EDS mapping shows a grain containing titanium with iron traces in the upper row and nine potassium feldspar grains in the lower row

In order to document statistical homogeneity of the medium, we sampled the replica in individual planes perpendicular to the principal directions and calculated the one-point probability function and its second central moment (variance), see Fig. 8. The courses of the $S_1^{(v)}$ function are found to be of random nature and the distances between local extremes and the expected mean, i.e., $\phi^{(v)} = 0.272515$, are quite small in magnitude, see also the variances in the caption of Fig. 8. We considered this observation to be a satisfactory proof of statistical homogeneity and proceeded with this assumption.

Microstructural characterisation by two-point correlation functions

Further microstructural characterisation was focused on the two-point correlation functions. Since sandstone rocks are supposed to have an anisotropic pore structure, we sampled the replica in the individual principal

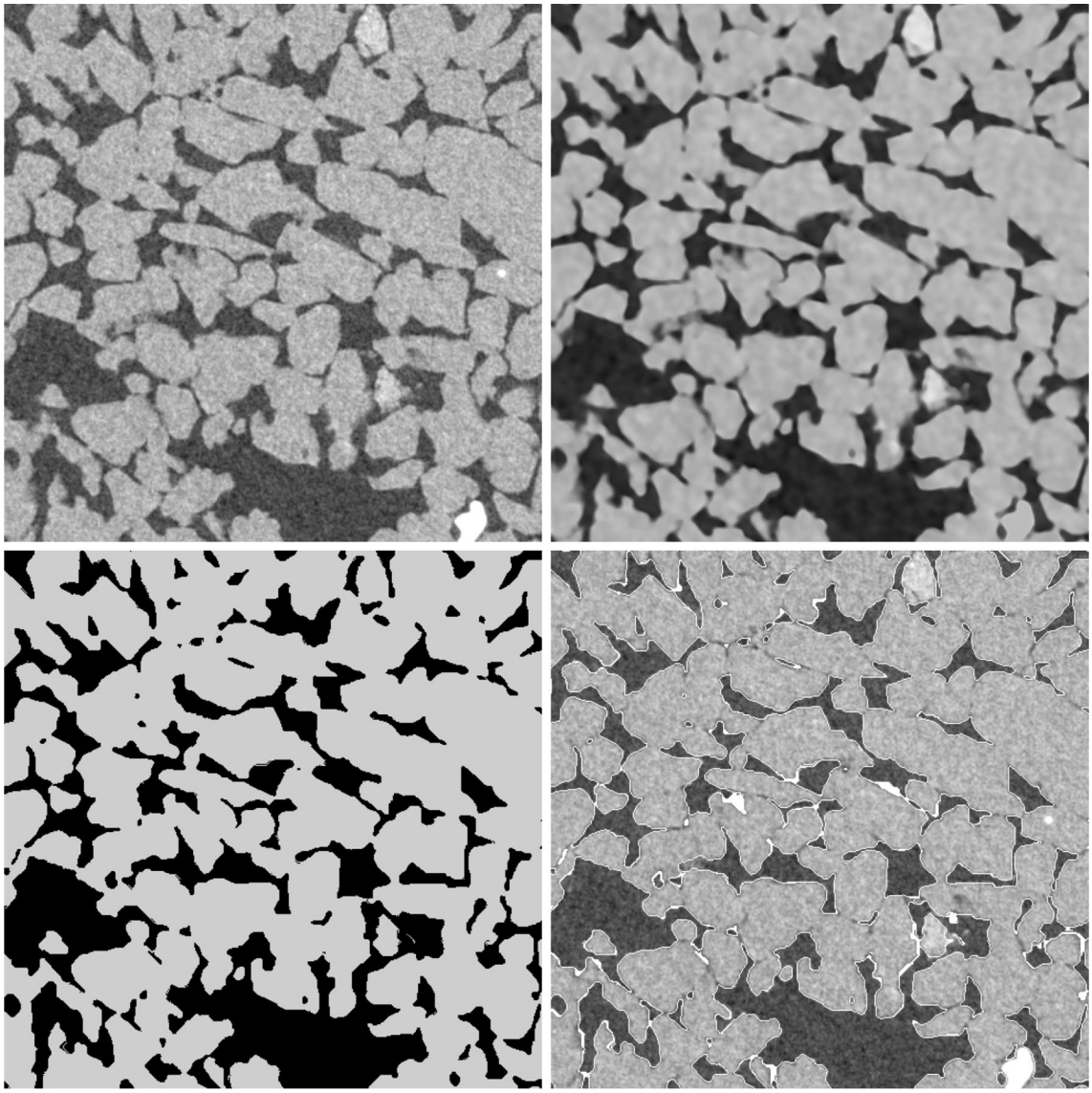

Fig. 6 2D images illustrating the effects of spatial filtering and segmentation of volume tomogram. The same region with a size of 512 × 512 pixels is shown for clarity. The raw and filtered images are displayed in the upper row, the segmented image and the combination of raw images with inscribed phase 3D interfaces (bright white curves) are shown in the lower row (pores are black). The phase interface can be thick when it represents a plane coinciding with the image plane. The pixel/voxel size *a* is 2.59 µm

directions and calculated the related two-point correlation and chord-length density functions. A preliminary inspection of the two-point probability function for the void phase and the two-point cluster function for the same phase confirmed that both descriptors were almost identical, which indicated the complete connectivity of all pores in accordance with the cluster analysis (cf. Figure 9 and Table 3). Subsequent inspection of the courses of the descriptors along the three principal directions showed that there were substantial differences between the *z*-principal direction (collinear with longitudinal axis of the cylindrical specimen) and the *x*- and *y*-principal directions (collinear with two arbitrary radial directions of the specimen). Since the black curve lay below the red and blue curves almost everywhere, the long-range connectivity of pore space in the axial (*z*-) direction was weaker than in the two others. It is worth noting that the two-point cluster function is capable of recording the long-range connectivity of any phase independently of shape and size of its clusters. By contrast, the chord-length density functions measure short-range connectivity along line segments that are collinear with the principal directions and, thus, can make a statistical survey of pore shapes in any principal direction. The chart

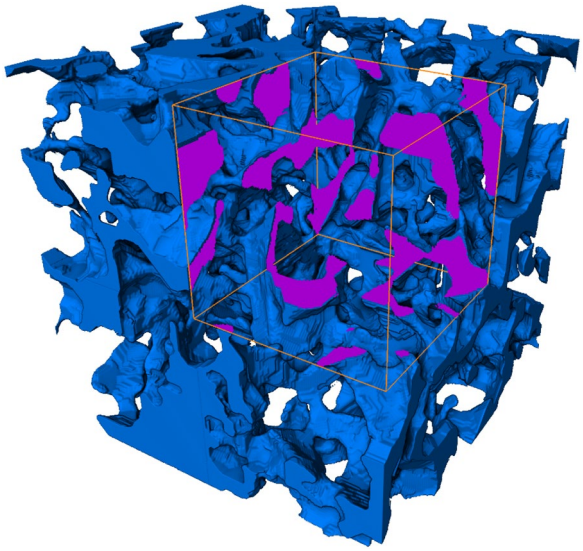

Fig. 7 Volume rendering of the pore space (blue). The orange box bounds a removed volume from the rendering, revealing the typical pore cross sections (purple). The solid phase is transparent. The size of the region is 256 × 256 × 256 voxels, i.e., 663 × 663 × 663 μm^3

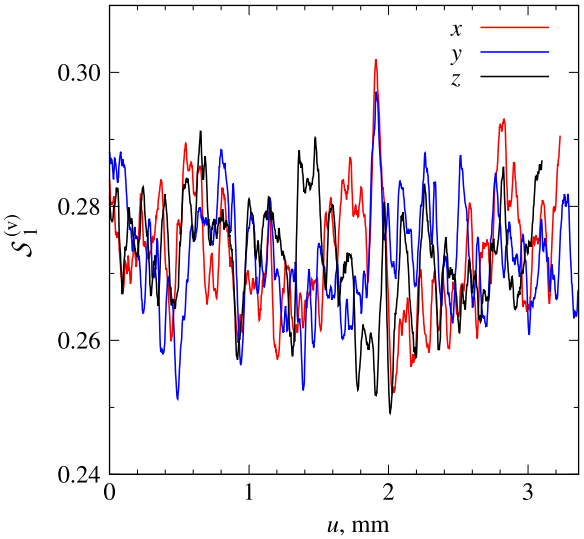

Fig. 8 One-point probability functions for the void phase sampled in individual planes perpendicular to the principal directions. The second central moments of $S_1^{(v)}$ along the *x*, *y* and *z* directions are 8.00×10^{-5}, 6.35×10^{-5} and 6.58×10^{-5}, respectively

on the right-hand side of Fig. 9 supports the existence of more-or-less regular pore shapes, at least without any significant elongation of pores in any principal direction. Therefore, it was very likely that different long-range connectivity of pore space rather than different morphology of pores was responsible for anticipated unidirectional differences in macroscopic properties.

Besides the $C_2^{(v)}$ function, connectivity of the pore space can further be assessed by means of the LPT descriptors. Although the local porosity distribution and the local percolation probability could be evaluated at any size Λ, it was convenient to simplify the analysis of the statistically homogeneous porous medium and to choose a special length Λ^* at which $\Phi(\phi, \Lambda)$ vanished at $\phi = 0$ and $\phi = 1$: $\Lambda^* = \min(\Lambda : \Phi(0, \Lambda) = \Phi(1, \Lambda) = 0)$.

This meant that no measurement cell of size Λ^* fit into any part of the void phase or the solid phase. The top left chart of Fig. 10 depicts the local porosity distribution that resembles the normal distribution because it is almost symmetric and because it has small differences among the first moment, the median and the modus, particularly 0.27251, 0.25959 and 0.25781, respectively. The distribution is also quite narrow, according to a second central moment (variance) of 3.66×10^{-3}. The pore space of most of the measurement cells was well connected, which was deduced from the right upper and bottom charts of Fig. 10. If the local porosity reached an approximate value of 0.2, the measurement cell percolated simultaneously along all three principal directions with the probability approaching one, i.e., $K_3(\phi, \Lambda^*) \to 1$, and the local percolation probability $K_i(\phi, \Lambda^*)$ was more or less independent of direction *i*. Differences among the principal directions were supposed to appear when $\Lambda < \Lambda^*$. This was corroborated by the courses of the total fraction of percolating cells $Q_i(\Lambda)$ for which the following relations held true: $Q_x(\Lambda) > Q_z(\Lambda) \wedge Q_y(\Lambda) > Q_z(\Lambda)$, see Fig. 10. Since the differences were mild and, thus, the pore space was mildly anisotropic, we did not suppose the transport properties to be highly macroscopically anisotropic.

The "pore-size" distribution functions represent intrinsically three-dimensional descriptors which are mathematically well-defined, unlike the pore-size distribution obtained from the mercury intrusion curve [16]. In Fig. 11 it is evident that most of the spherical regions in the solid and void phases have radii smaller than 80 and 50 μm, respectively. The $P^{(s)}$ function

Table 3 Cluster analysis of the primary replica expressed as total volume fractions, $\varphi^{(s)}$ and $\varphi^{(v)}$, of the solid and void phases and volume fractions of percolating, internal isolated, and external isolated clusters of voxels for both phases

	Total	Percolating	Internal isolated	External isolated
solid	0.727484	0.727268	1.67×10^{-4}	4.9×10^{-5}
void	0.272516	0.272286	1.87×10^{-4}	4.3×10^{-5}

The percolating cluster (of solid voxels) means that the cluster spans the whole replica in all three principal directions

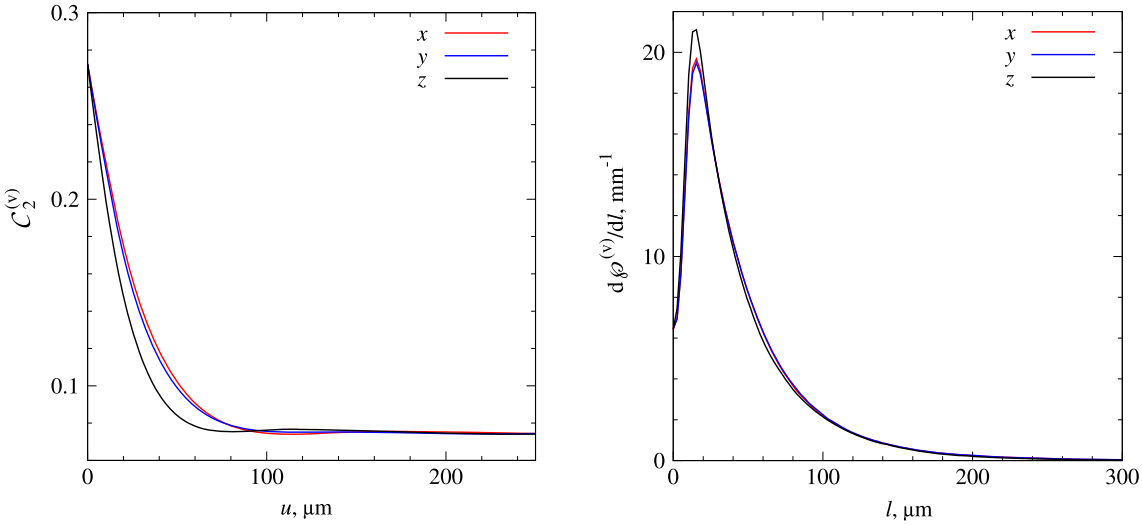

Fig. 9 Left: The two-point cluster function for the void phase. Right: The chord-length density functions for void phase. The functions are measured along the principal directions. The mean chord lengths in the individual directions are 46.3, 46.9 and 43.9 μm, respectively

exhibits a characteristic flattened part between 3 and 12 μm that forms as a result of the existence of large, regularly shaped pores (cavities) interconnected with narrow throats. Numerous spherical regions lying between cavities and in the vicinity of throats contribute to this flattened part of $P^{(s)}$. An indication of the flattened part of $P^{(v)}$ can be observed in the right-hand chart of Fig. 11, which can be accounted for by the same cause.

Histograms of sizes

While the "pore-size" distribution functions record Euclidean distances between a randomly chosen point in a phase and the closest phase interface, the measures characterising the partitioned regions are closer to the common perception of pore and grain sizes. Both histograms depicted as the relative frequencies as functions of cube root of the grain and pore volumes, V_g and V_p, resemble the normal distributions that are positively skewed. In both cases the positive skewness is caused by a rare occurrence of voluminous outliers, the largest of which are not included in the top row of Fig. 12. The histogram related to the solid phase was treated as unimodal with a fairly sharp maximum corresponding to 65335 voxels ($V_g \approx 1.13 \times 10^6$ μm^3). One isolated box at the very beginning represented the unconnected solid voxels located at the external sides of the cuboid replica (see the second paragraph in this section). In the void phase there were no isolated one-voxel clusters as deduced from the void-phase histogram that is clearly unimodal with a flat maximum between 6020 and 13240 voxels, i.e., $V_p \in [1.04 \times 10^5;\ 2.29 \times 10^5]$ μm^3 or, equivalently, $V_p^{1/3} \in$ [47; 61] μm. When the partitioned regions are assessed in terms of the volume fractions and the region radii (3), the histograms exhibit more pronounced positive skewness due to the higher weight of large regions. The solid-phase distribution has a mode of 71 μm and few boxes related to grains as large as 216 μm in radius, while the long tail and the flat maximum between 43 and 51 μm characterise the histogram of the partitioned pore space (Fig. 12, bottom row).

Traditionally, the pore structure is described using the concept of pore throats located at narrow regions that form connections between adjacent pores. In Fig. 13 the two histograms depict the relative number of occurrences of pore throats either as a function of square root of the throat area A_t or as a function of the ratio of the throat area A_t to the total pore surface area A_p. The former histogram has a flat maximum with a mode between 20 and 24 μm and a mean value of 33.1 μm. These values are, in fact, the side length of the squares of the associated areas. If their halves are taken into account, both values are directly comparable with the "pore-size" distribution obtained from mercury porosimetry, which has a maximum of around 13.7 μm (Fig. 2). The apparent link between the directly observed throat sizes and the mercury intrusion data has the straightforward explanation: while the intrusion curve is sensitive to throat sizes and associates them with pore volumes, the partitioned regions represent pores (cavities) rather than constrictions (necks) connecting pores. The latter histogram demonstrates the significant convergent-divergent nature of the pore space, since the throat size covers at most one half of the total surface area per pore (cavity).

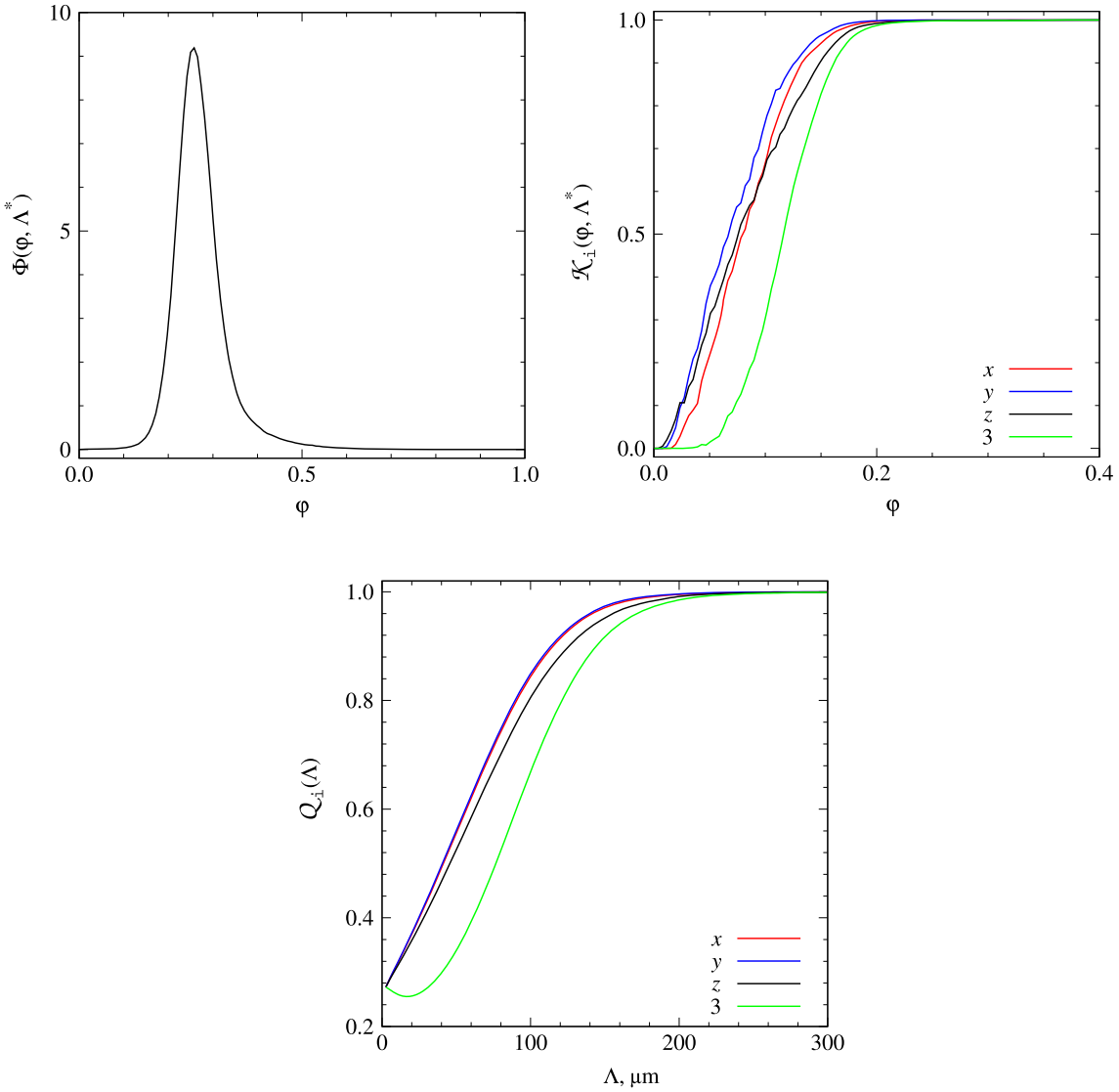

Fig. 10 Top: The local porosity distribution and the local percolation probability evaluated using the measurement cell of special size 85 voxels (Λ* = 220 μm). Bottom: The total fraction of percolating cells as a function of Λ. Direction 3 means that simultaneous percolation in all three principal directions of the cubic measurement cell is observed

Other description of the space topology

Pore space topology can further be described by evaluating the coordination numbers, c_n, of the partitioned pore space (Fig. 14, right). The corresponding probability mass function reaches its maximum value at $c_n = 4$ and has positive skewness with rare outlier values as large as 53. The extremely high coordination numbers were caused by a few very large pores that had many neighbours. A mode of 4, the mean coordination number $\langle c_n$ equal to 5.48, and the relatively low frequency of pores with $c_n \leq 1$ also confirmed the observation made earlier pertaining to the two-point cluster function $C_2^{(v)}$ and the percolation probabilities $K_i(\phi, \Lambda^*)$ and $Q_i(\Lambda)$ (Figs. 9 and 10). These findings mean that several different fluid threads in the pore space are very likely to connect each internal pore with the external fluid and that entrapment of a fluid wetting the sandstone less than another fluid, e.g., air when a consolidating agent imbibes the pore space, should be of minor extent. By analogy, the distribution of coordination numbers of grains was estimated (Fig. 14, left). The distribution reaches the maximum at a coordination of 8 with a median coordination of approximately 8 and a mean coordination of 8.74. The tail of the distribution extends to a coordination of 62; however, fewer than 4%

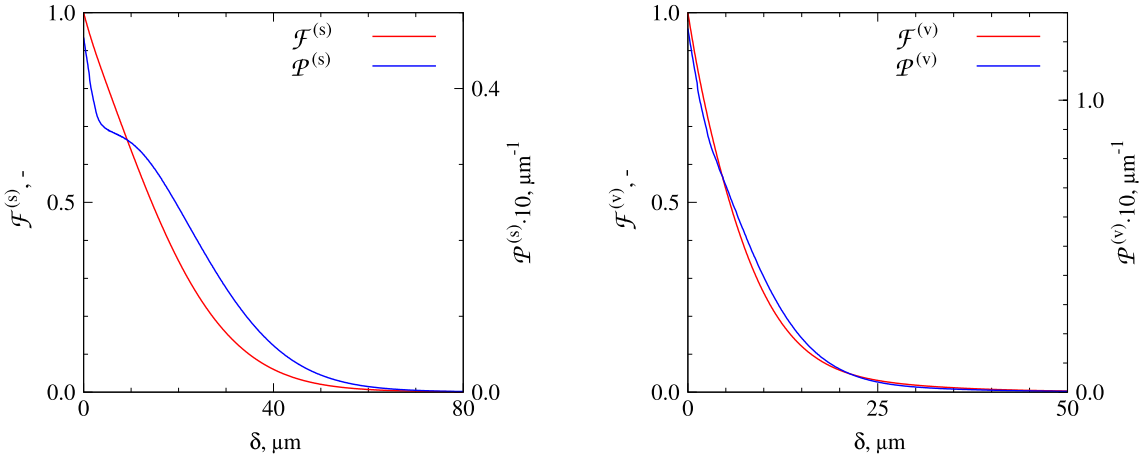

Fig. 11 Probability density functions, $P^{(i)}$, and complementary cumulative distribution functions, $F^{(i)}$, for the solid and void phases. Note that the relationship $P^{(i)}(0) = s/\varphi^{(i)}$ complemented random sampling of the cuboid region

of grains show a coordination above 16 and fewer than 10% have a coordination above 13.

Effective transport properties

By solving the Stokes equations (Eq. (6 and 7) in the Additional file 1) together with the appropriate boundary condition, we obtained the local velocity and pressure fields. Their inspection can provide interesting information about the most permeable paths or bottlenecks of the pore structure, see Fig. 15. For instance, dark orange/red regions represent pores in which the fluid moves against the macroscopic direction of flow, i.e., there is a local negative velocity. There are also a few relatively narrow pores where the velocity is high. These pores are likely to be part of highly permeable paths in the pore structure. However, the excess of information contained in the 3D fields is usually reduced and, as a result, effective transport properties are obtained. By contrast, the random walk simulations are designed to yield effective properties directly.

Here, the effective transport properties calculated for the Knudsen and continuum limits are summarised in Table 4, where only the diagonal elements of both tensors are included. This simplification was justified because the non-diagonal elements were at least one order of magnitude below the smallest diagonal element. In accordance with the microstructural analysis, the main diagonal elements in the radial directions of the tomographic specimen (β_{ii} and κ_{ii}, $i=1, 2$) were greater than those in the axial direction (β_{33}, κ_{33}). For instance, the two-point cluster functions clearly exemplified that pores were connected more weakly in the axial (z) direction than in the other two directions (cf. the black, red and blue curves in Figs. 9 and 10). In addition, the total fraction of percolating cells $Q_i(\Lambda)$ also predicted the reduced connectivity of pore space in the axial direction (Fig. 10, bottom chart). Comparing ratios of the diagonal elements in Table 4 shows that the relative reduction is approximately the same (≈88%) in the Knudsen and continuum limits. Therefore, we concluded that gas flow through the specimen was mildly macroscopically anisotropic.

Experimental counterparts of the simulated effective properties were estimated from a set of pressure relaxations in the permeation cell (Additional file 1: Fig. S1 in the SI). Examples of $p(t)$ measured at both bounds of the mean pressure interval are shown in Fig. 16. In accordance with the theory, the pressure difference relaxed most slowly at the lowest equilibrium pressure P_∞ in the cell, while the fastest relaxation taking about 60 s was observed at the upper pressure bound. The course of the shortest response also explains why a maximum equilibrium pressure of 55 kPa was used. A possible increase of the equilibrium pressure P_∞ above 55 kPa would accelerate a pressure difference relaxation even more and would strengthen the effect of dynamical phenomena on the course $p(t)$. The minimization of χ^2 was straightforward because less than ten iterations of the Levenberg–Marquardt method were necessary to achieve the minimum when initial estimates within the intervals [0.01, 1] μm and [0.01, 10] μm^2 were used for κ_e and β_e, respectively. The ease of finding the global minimum of χ^2 supported our assumption that the collected data sets were rich in information. The best (point) estimates of κ_e and β_e in the sense of the least-squares methods and their joint confidence intervals are summarised in Table 5. By contrast, the best estimates of $p_{0,j}$ were omitted because they were very close to those measured experimentally and because they would be of no use for further discussion.

To better demonstrate the stability of the best estimates of κ_e and β_e, we repeatedly minimised the objective

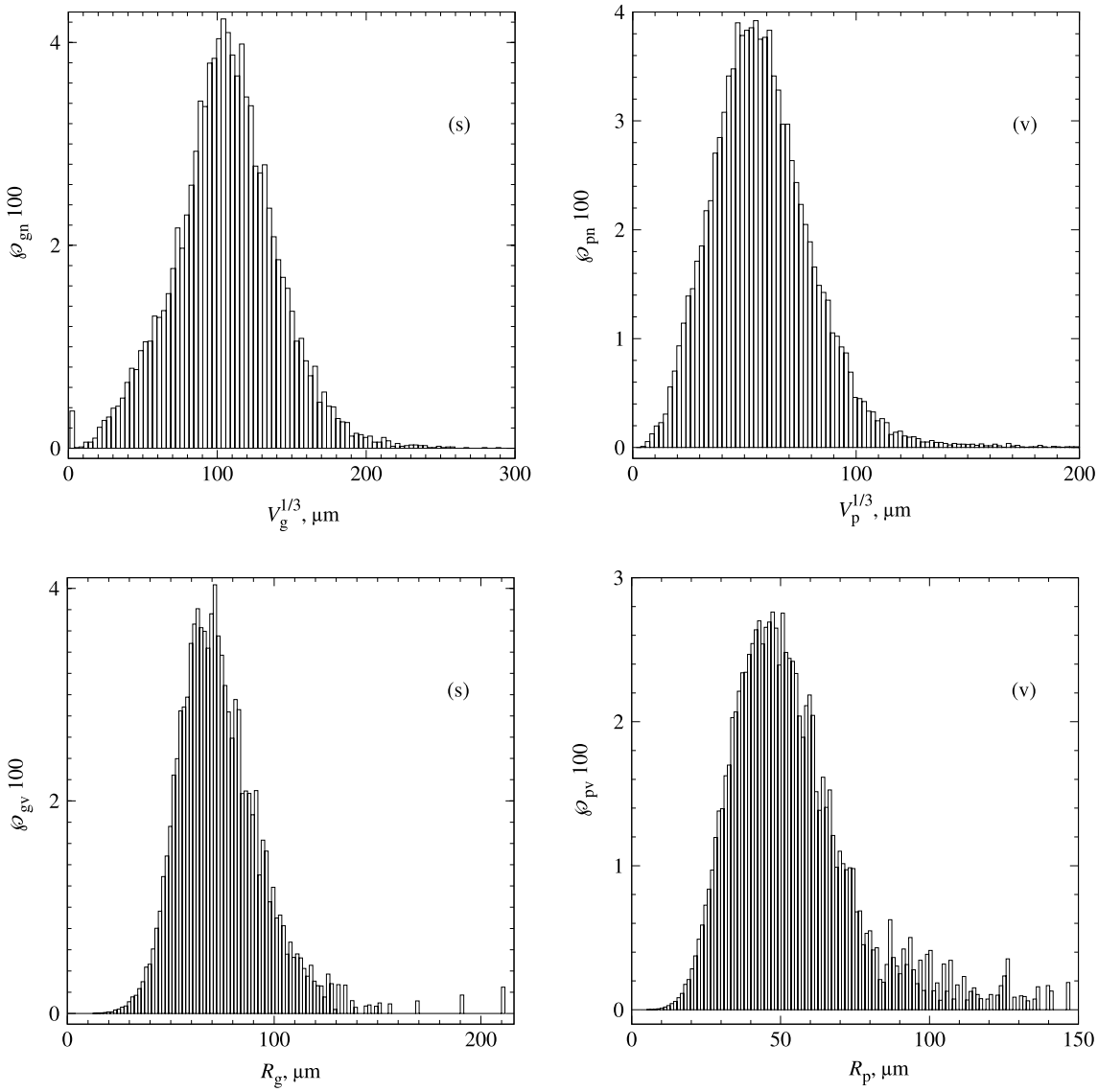

Fig. 12 Histograms of sizes of the partitioned phases: solid (s) and void (v). In the upper row, the relative frequencies (relative number of occurrences, $\wp_{gn}$ and $\wp_{pn}$) as functions of cube root of grain and pore volumes ($V_g^{1/3}$ and $V_p^{1/3}$) are shown. A few very voluminous outliers are omitted to improve resolution. In the lower row, there are the volume fractions ($\wp_{gv}$ and $\wp_{pv}$) as functions of the characteristic radii of grains and pores (R_g and R_p shown in the full range)

function (Eq. (10), see Additional file 1 SI) that included the separated responses for nitrogen (first row in Table. 5) and argon (second row) and the combined responses for nitrogen and argon (third row). The joint confidence regions of all variables were determined using the χ^2 function linearized in the vicinity of the best estimates of κ_e, β_e and $p_{0,j}$. According to the recommendation by Press et al. (1992), the goodness-of-fit G was calculated using the upper incomplete gamma function Γ, i.e.,

$$G = \Gamma\Big(\big(\omega - 2\updownarrow - 2\big)/2, \chi^2_{\min}/2\Big),$$

where $\omega = \sum_{j=1}^{\updownarrow} k_j$ stands for the total number of data pairs $[t, p^e]$ and $\omega - 2\ell - 2$ is the number of degrees of freedom.

The values of G in Table. 5 suggested that the mathematical model of the cell (Eq. (9), see Additional file 1 SI) and both parameters κ_e and β_e were believable. A closer inspection of Table. 5 revealed that the transport parameter β_e was estimated more reliably than the parameter κ_e. This anticipated difference was related to the limited interval of P_2 in which the experiments could be conducted. Since the sandstone was macroporous, the prevailing transport

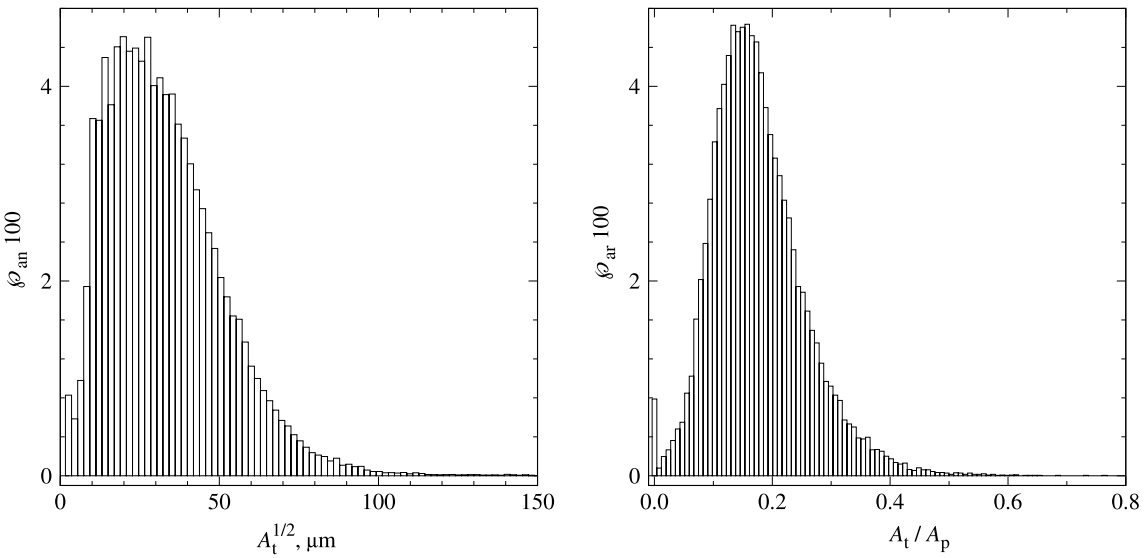

Fig. 13 Histograms of throat sizes of the partitioned pore space. Left: The relative frequency (relative number of occurrence $\wp_{an}$) as a function of square root of the throat area ($A_t^{1/2}$). A few very large outliers are omitted to improve resolution. Right: The relative frequency $\wp_{ar}$ as a function of the ratio of the throat area A_t to total pore surface area A_p

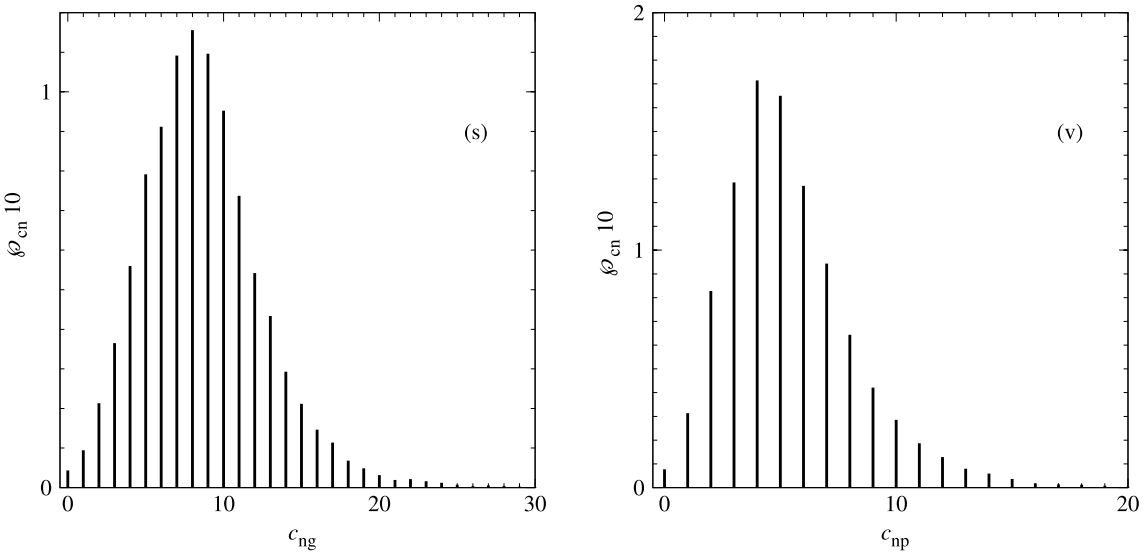

Fig. 14 Probability mass functions of the coordination number c_n of the partitioned regions: (left) the solid phase and (right) the pore space. Outliers beyond 30 and 20 are omitted to improve the resolution of the left and right charts, respectively

mechanism was viscous flow. Although the experiments made at the lower bound of the P_2 interval shifted the mass transport to the Knudsen region, the Knudsen flow did not dominate the total transport and, consequently, the parameter κ_e associated with the Knudsen region was loaded by higher uncertainty. Note that a further decrease of the total pressure, which would resolve this issue, would require another pair of pressure transducers to monitor very low pressures in the cell.

In summary, we considered deviations between the calculated and experimental data in Tables. 4 and 5 to be acceptable, bearing in mind that the specimens for tomography and permeation were different and that the confidence regions of κ_e and β_e exclusively followed from uncertainty about determination of the pressure difference. If uncertainties about other parameters, such as the pellet height and diameter, temperature and the chamber volumes, were taken into account, the confidence regions

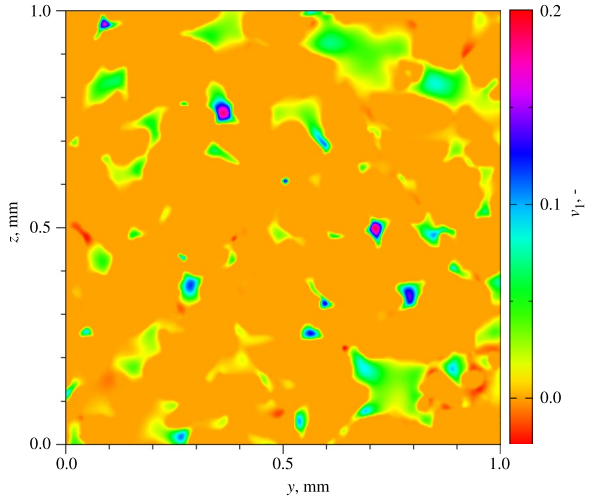

Fig. 15 Viscous flow in the plane perpendicular to the *x*-axis when the pressure difference is exerted in the same direction. The first velocity component $v_1(\boldsymbol{x})$ is mapped onto the plane by projecting its relative values. An area of 1 mm^2 is shown for the sake of clarity. Naturally, the velocity component v_1 is zero in the solid-phase region

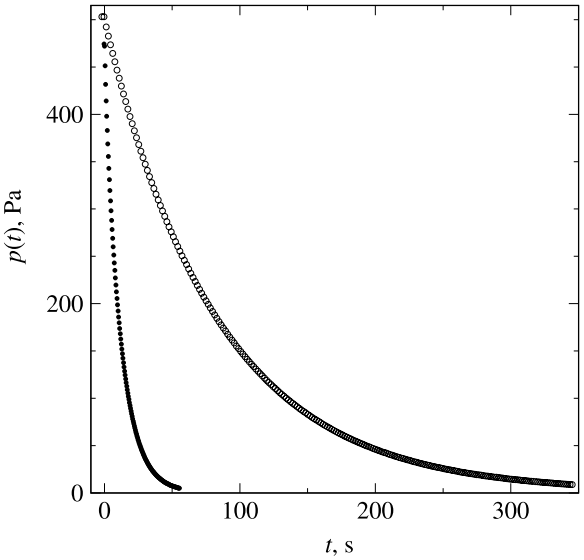

Fig. 16 Examples of two measured pressure differences as a function of time, i.e., $p(t)$, for argon. The parameter of the curves is the initial pressure in chamber 2: (o) $P_2(0) = 3.90$ kPa, $p_0 = 500$ Pa and (•) $P_2(0) = 52.63$ kPa, $p_0 = 474$ Pa. Most of the points were omitted to allow for individual points to be visible

would be wider and the agreement between the theory and the experimental data would be apparent. Consequently, we considered the pore-scale model to be representative of the real material.

Conclusions

Our study provided two important outcomes concerning the porous system of the Msene sandstone, which is one of the most common materials of the heritage buildings and artifacts. First, both the preliminary tests based on water imbibition and X-ray computed microtomography suggested that the rock microstructure is statistically homogeneous and almost isotropic on a macroscopic length scale. Second, even if the pore structure was found to be fully connected with minor occurrence of dead-end pores, due to the significant narrowing of pores followed by their widening, an empirical prediction of imbibition of the consolidant is difficult. While good pore-space connectivity suppresses trapping of the non-wetting phase (air), constrictions in the pore space can support creating blobs of air in large pores (cavities). The modelling of the

Table 4 Summary of diagonal elements of the effective permeability tensor β_{ji}, all expressed in [μm^2], and scaled diagonal elements of the effective diffusivity tensor in the Knudsen region κ_{ij} given by Eq. (5) (see Additional file 1 SI), all expressed in [nm]

β_{11}	β_{22}	β_{33}	$\overline{\beta}$	κ_{11}	κ_{22}	κ_{33}	$\overline{\kappa}$
3.49	3.57	3.10	3.39	873	903	787	854

$\overline{\beta} = (\beta_{11} + \beta_{22} + \beta_{33})/3$ and $\overline{\kappa} = (\kappa_{11} + \kappa_{22} + \kappa_{33})/3$

Table 5 Effective transport parameters κ_e and β_e and their confidence regions $\sigma(\kappa_e)$ and $\sigma(\beta_e)$ evaluated for a confidence level of 95.45%, the minima of χ^2 and the goodness-of-fit G

Run\quantity	ℓ	ω	κ_e, nm	$\sigma(\kappa_e)$, nm	β_e, μm^2	$\sigma(\beta_e)$, μm^2	χ^2_{min}	G
N_2	7	1519	1290	±190	3.992	$\pm 7.8 \times 10^{-2}$	1180	1.000
Ar	10	2102	1170	±180	4.058	$\pm 8.9 \times 10^{-2}$	2175	0.072
N_2, Ar	17	3613	1220	±160	4.024	$\pm 7.4 \times 10^{-2}$	3324	0.999

The standard deviation σ_p was 0.33 Pa for all data pairs

consolidant penetration based on the detailed quantitative description of the stone porosity, which was obtained by the methods presented in our communication, can be very helpful in the development of novel consolidants.

Supplementary Information

The online version contains supplementary material available at https://doi.org/10.1186/s40494-022-00854-8.

Additional file 1: **Table. S1**. Results of water absorbability for ten sandstone specimens: the bulk density ρ_w, the open porosity φ_w and the specific volume V_p. Specimen E was used for tomographic reconstruction and other measurements. **Fig. S1**. Diagram of the permeation cell. 1 – impermeable disc with one cylindrical opening, 2 – cylindrical pellet, 3 – lower cell compartment, 4 – upper cell compartment, 5 – lower container, 6 – upper container, 7 – relative pressure gauge, 8 – differential pressure transducer, 9 – inlet needle valve, 10 – ball valve for experiment triggering, 11 – bypass ball valve, 12 – outlet needle valve. $V_1 = 988$ mL, $V_2 = 1131$ mL, $h = 5.00$ mm and $d = 5.69$ mm.

Acknowledgements
The authors acknowledge the assistance provided by the Research Infrastructures NanoEnviCz (Project No. LM2018124) supported by the Ministry of Education, Youth and Sports of the Czech Republic and the project Pro-NanoEnviCz (Reg. No. CZ.02.1.01/0.0/0.0/16_013/0001821) supported by the Ministry of Education, Youth and Sports of the Czech Republic and the European Union—European Structural and Investments Funds in the frame of Operational Programme Research Development and Education for providing access to the Micromeritics 3Flex apparatus.

Author contributions
PC: conceptualisation, methodology, programming the related software, evaluating experimental data, measuring permeability, writing—original draft, writing—review & editing, supervision. MV: back-scattered electron imaging, chemical composition analysis, visualisation and writing—review & editing. MS: x-ray computed micro-tomography and creating volume image. MR: Methodology, investigation. RZ: writing—review & editing. MK: investigation, data curation. JR: conceptualisation, funding acquisition, project administration, supervision. LB: writing—review & editing. All authors approved the manuscript.

Funding
The research was supported by the Academy of Sciences of the Czech Republic within the program Strategy AV21 No. 23—The City as a Laboratory of Change; buildings, cultural heritage and an environment for a safe and valuable life.

Availability of data and materials
The datasets used and/or analysed during the current study are available from the corresponding author on reasonable request.

Declarations

Competing interests
The authors declare that they have no competing interests.

Received: 23 August 2022 Accepted: 27 December 2022
Published online: 21 February 2023

References

1. Remzova M, Sasek P, Frankeova D, Slizkova Z, Rathousky J. Effect of modified ethylsilicate consolidants on the mechanical properties of sandstone. Constr Build Mater. 2016;112:674–81.
2. Remzova M, Carrascosa L, Mosquera M, Rathousky J. Modified ethylsilicates as efficient innovative consolidants for sedimentary rock. Coatings. 2018;9:6.
3. Remzova M, Zouzelka R, Brzicova T, Vrbova K, Pinkas D, Rőssner P, et al. Toxicity of TiO2, ZnO, and SiO2 nanoparticles in human lung cells: safe-by-design development of construction materials. Nanomaterials. 2019;9:968.
4. Miliani C, Velo-Simpson ML, Scherer GW. Particle-modified consolidants: a study on the effect of particles on sol–gel properties and consolidation effectiveness. J Cultural Heritage. 2007;8:1–6.
5. Remzova M. Nanostructured systems for the consolidation of historical objects, PhD Thesis. Prague: University of chemistry and technology; 2019.
6. Remzova M, Zouzelka R, Lukes J, Rathousky J. Potential of advanced consolidants for the application on sandstone. Appl Sci. 2019;9:5252.
7. Rybařík V. Ušlechtilé stavební a sochařské kameny České republiky. Nadace střední průmyslové školy kamenické a sochařské: Hořice v Podkrkonoší (Czech Republic); 1994.
8. Latt J, Malaspinas O, Kontaxakis D, Parmigiani A, Lagrava D, Brogi F, et al. Palabos: parallel lattice boltzmann solver. Comput Math with Appl. 2021;81:334–50.
9. Dullien FAL. Porous media: fluid transport and pore structure. 2nd ed. San Diego: Academic Press Inc; 1992.
10. Weickert J. A review of nonlinear diffusion filtering. In: ter Haar Romeny B, Florack L, Koenderink J, Viergever M, editors. Scale-Space Theory in Computer Vision Scale-Space Lecture Notes in Computer Science. Berlin: Springer; 1997.
11. Weickert J, Romeny BMTH, Viergever MA. Efficient and reliable schemes for nonlinear diffusion filtering. IEEE Trans Image Proc. 1998;7:398–410.
12. Welk M, Steidl G, Weickert J. Locally analytic schemes: a link between diffusion filtering and wavelet shrinkage. Appl Comput Harmonic Anal. 2008;24:195–224.
13. Weickert, J., Grewenig, S., Schroers, C., Bruhn A. Cyclic Schemes for PDE-Based Image Analysis. FR 61 – Mathematik Preprint No 327 (revised). Saarbrücken, Germany: Universität des Saarlandes; 2015.
14. Couprie C, Grady L, Najman L, Talbot H. Power watershed: a unifying graph-based optimization framework. IEEE Trans Pattern Anal Machine Intell. 2011;33:1384–99.
15. Vincent L. Morphological grayscale reconstruction in image analysis: applications and efficient algorithms. IEEE Trans Image Proc. 1993;2:176–201.
16. Torquato S. Random heterogeneous materials: microstructure and macroscopic properties. New York: Springer; 2002.
17. Fott P, Petrini G. Determination of transport parameters of porous catalysts from permeation measurements. Appl Catalysis. 1982;2:367–78.

Publisher's Note